UDC 621.3 https://doi.org/10.20998/2074-272X.2025.6.09

V.T.K. Nhi, B.T. Quy, H.H.B. Nghia, L.V. Dai

A robust hybrid control strategy for enhancing torque stability and performance in PMSM drives

Introduction. *Recently, permanent magnet synchronous motors (PMSMs) have become essential in various high-performance applications, including electric vehicles and renewable energy systems. However, traditional control methods, such as PI controllers, often struggle to handle dynamic operating conditions and external disturbances, resulting in torque ripple and stability issues.* ***Problem.*** *The main issue with existing control strategies is their inability to maintain accurate torque control and system stability under fluctuating loads and varying motor parameters, which negatively impacts performance in real-world applications.* ***Goal***. *This paper proposes a robust hybrid control strategy that integrates sliding mode control (SMC) with proportional resonant control (PRC), enhanced by Luenberger and Kalman observers. The goal is to improve torque stability, reduce errors, and optimize performance in PMSM drive systems.* ***Methodology***. *The proposed method combines SMC and PRC to form an SMC-PRC controller, with Luenberger and Kalman observers integrated for effective load torque estimation.* ***Results***. *The simulation experiments were carried out to compare the effectiveness of the proposed control strategy with that of traditional PI controllers. The results revealed that the SMC-PRC approach offers a notable improvement in overall control performance, including reduced tracking error, enhanced dynamic response, and better stability. Furthermore, the proposed method achieved faster settling times and maintained robust operation under varying system conditions.* ***Scientific novelty***. *This work introduces a hybrid control approach that combines SMC and PRC with advanced state estimation techniques, providing a robust and efficient solution to PMSM control.* ***Practical value***. *The proposed method is highly beneficial for applications under dynamic operating conditions, such as electric vehicles and renewable energy systems, improving system efficiency and stability*. References 40, tables 7, figures 10.

Key words: **permanent magnet synchronous motor, sliding mode control, proportional resonant control, integral absolute error, integral time absolute error, integral square error, Luenberger observer, Kalman filter.**

Вступ. *Останнім часом синхронні двигуни з постійними магнітами (PMSM) стали невід'ємною частиною різних високопродуктивних застосувань, включаючи електромобілі та системи відновлюваної енергії. Однак традиційні методи управління, такі як ПІ-регулятори, часто не справляються з динамічними робочими умовами та зовнішніми збуреннями, що призводить до пульсацій крутного моменту та проблем зі стабільністю. Основною* ***проблемою*** *існуючих методів управління є їх нездатність підтримувати точне управління крутним моментом і стійкість системи при коливаннях навантаження і параметрах двигуна, що змінюються, що негативно впливає на продуктивність в реальних ситуаціях.* ***Мета***. *У цій статті пропонується надійна гібридна стратегія управління, що поєднує управління ковзним режимом (SMC) з пропорційно-резонансним управлінням (PRC), удосконалена за допомогою спостерігачів Люенбергера та Калмана. Мета полягає в тому, щоб підвищити стабільність крутного моменту, зменшити похибки і оптимізувати продуктивність систем приводу PMSM.* ***Методологія***. *Пропонований метод об'єднує SMC та PRC для формування регулятора SMC-PRC, з інтегрованими спостерігачами Люенбергера та Калмана для оцінки ефективного крутного моменту навантаження.* ***Результати***. *Проведено імітаційні експерименти порівняння ефективності запропонованої стратегії управління з ефективністю традиційних ПІ-регуляторів. Результати показали, що підхід SMC-PRC забезпечує помітне покращення загальних характеристик управління, включаючи зниження похибки стеження, покращення динамічного відгуку та підвищення стійкості. Крім того, пропонований метод забезпечує більш швидкий час встановлення і стійку роботу при умовах функціонування системи, що змінюються.* ***Наукова новизна***. *У роботі представлений гібридний підхід до управління, що поєднує SMC та PRC з передовими методами оцінки стану, що забезпечує надійне та ефективне рішення для управління PMSM.* ***Практична значимість***. *Запропонований метод є корисним для застосування у динамічних умовах експлуатації, таких як електромобілі та системи відновлюваної енергії, підвищуючи їх ефективність та стійкість.* Бібл. 40, табл. 7, рис. 10.

Ключові слова: **синхронний двигун з постійними магнітами, керування ковзним режимом, пропорційно-резонансне керування, інтегральна абсолютна похибка, інтегральна тимчасова абсолютна похибка, інтегральна квадратична похибка, спостерігач Люенбергера, фільтр Калмана.**

Introduction. The permanent magnet synchronous motor (PMSM) is widely used in critical applications across various industries, including electric vehicles, industrial robotics, aerospace, and especially in the rapidly expanding renewable energy sector [1–3]. PMSMs offer key advantages such as high power density, exceptional efficiency, and a broad speed range, all of which contribute to their high reliability [4, 5]. PMSM control methods are generally categorized into 3 main approaches: field-oriented control (FOC), direct torque control (DTC) and V/F control [6, 7]. While DTC and V/F control are relatively simple to implement, they are prone to significant torque ripple and lower efficiency [8]. In contrast, FOC provides precise control of the magnetic field by adjusting the frequency, voltage, and inverter output position, which ensures stable torque, low noise, high power, and excellent dynamic performance [6, 9].

Linear control methods, such as PI control, PID control, and linear state feedback, have been commonly applied to control PMSMs. However, PMSMs exhibit numerous nonlinear characteristics, including system uncertainties and external disturbances, which increase the complexity of controller design. These nonlinearities also make it more challenging to achieve the desired tracking performance in PMSM control systems [10]. To address these challenges, nonlinear control methods such as sliding mode control (SMC), fuzzy logic control, adaptive control, and model predictive control have gained popularity. For example, articles [11, 12] explore integrating a fuzzy event-trigger mechanism with super-twisting SMC to enhance sampling efficiency and tracking performance. Additionally, disturbance observer-based SMC has been introduced to counteract external disturbances in PMSM control [13].

As a result, sensorless control algorithms for PMSMs have become a key research area in motor control. These algorithms include high-frequency injection, extended Kalman filters (EKFs), model reference adaptive systems, and sliding mode observers (SMO) [14, 15]. Among these, SMO has become a preferred method due to its advantages in variable-structure control systems, simple implementation, and high robustness against parameter variations and external

disturbances. Sensorless control methods primarily involve high-frequency signal injection [16] and the fundamental frequency model [17]. The high-frequency injection method involves injecting a high-frequency voltage or current into the system and analyzing the response to estimate rotor position, even when the motor is stationary or running at low speeds. However, this approach can introduce high-frequency noise, which impacts system performance. On the other hand, the fundamental frequency model is typically used for medium-to-high speed ranges, where the stator current is employed as input to an observer to determine rotor position. Common observers used in this method include the EKF [18, 19], model reference adaptive control [20], SMO [21] and a nonlinear flux observer [22, 23]. Among these, EKF has better convergence at low speeds but heavily depends on tuning the noise matrix to achieve high accuracy, requiring extensive simulation experiments to fine-tune suitable parameters [24].

Recently, optimization algorithms have been employed to determine the optimal values for the Q and R matrices in the EKF [24]. Several studies have utilized real-coded genetic algorithms in sensorless PMSM control systems to optimize the noise matrices of the EKF [25, 26]. Another approach involves the use of a normalized EKF, designed to improve the adaptability of the EKF to various control systems. This method integrates a swarm intelligence algorithm for offline parameter self-learning. However, these optimization algorithms come with high computational complexity, requiring large training datasets and multiple iterations to achieve optimal results, which results in extended training times. Additionally, ensuring that the training dataset sufficiently covers all possible operating conditions of the system remains a significant challenge in practical applications [24]. Some studies [27] have incorporated fuzzy logic into the EKF to adjust the Q and R noise matrices in the sensorless control system of PMSM. However, the effectiveness of this method is heavily dependent on the accuracy of the fuzzy logic control rules. Furthermore, other research [24, 28, 29] has applied the Sage-Husa Kalman algorithm to sensorless control systems of PMSM and linear PMSMs. This approach uses the Sage-Husa noise estimator to compute R via regression methods and determine Q. However, the traditional Sage-Husa noise estimator may lead to observer divergence. As a result, recent improvements have focused on enhancing the stability and accuracy of the observer, while preserving the benefits of fast convergence and high adaptability [24].

This study proposes a linear state estimation approach for load estimation of PMSM based on an improved Luenberger observer and a Kalman filter, incorporating the principles of the SMC for speed loop control and 2 proportional resonant control (PRC) controllers for current loop control. The proposed system aims to create a robust motor control system for surface-mounted PMSM (SPMSM) with precise state estimation, strong speed control, and stable current control, optimized for high-performance applications in environments with noise and load variations. The Kalman filter is utilized to estimate unmeasured states and filter the measured signals. This filter is a common choice in industrial applications due to its optimal performance in linear systems with zero-mean, uncorrelated Gaussian noise. Interestingly, the Kalman filter remains optimal even when the noise is non-Gaussian [30]. The Luenberger observer offers notable advantages, such as simplicity and low computational cost, particularly for linear systems. It is easy to implement and does not require complex calculations like the Kalman filter, allowing for quick and efficient state estimation. The estimated signal is then used for direct torque load compensation to enhance the system's instantaneous response. The SMC algorithm is introduced to reduce oscillation during sliding mode operation and improve system stability. This algorithm utilizes continuous control signals to replace traditional high-gain switching terms, thereby enhancing robustness against speed variations. Additionally, the algorithm integrates adaptive feedback gain correlated with the motor speed, mitigating the effects of speed fluctuations on system performance.

The **goal** of the paper is to propose a robust hybrid control strategy for PMSM drive systems, specifically targeting improved torque stability and overall system performance. By integrating SMC with PRC, the strategy seeks to minimize torque ripple and enhance system efficiency. The approach is further reinforced by the use of enhanced Luenberger state observer (LSP) and Kalman state observer (KSP) for accurate load torque estimation. The ultimate goal is to offer a more reliable, robust and efficient control solution, surpassing traditional PI controllers, particularly in environments with fluctuating loads and dynamic motor parameters.

Main contributions of this study are:

1. The proposal of a hybrid control strategy combining SMC and PRC, improving both torque stability and system performance, resulting in better performance than traditional PI controllers.
2. The integration of Luenberger and Kalman observers enhances load torque estimation and improves system reliability by accurately estimating unmeasured states.
3. The introduction of feed-forward compensation (FFC), which compensates for changes in load torque and disturbances, thus reducing delays and enhancing transient response.
4. Significant improvements in key performance metrics (integral of absolute error – IAE, integral of time-weighted absolute error – ITAE, integral of squared error – ISE) based on simulation results, showing reductions of up to 94.614 % in IAE, 94.603 % in ITAE and 99.708 % in ISE compared to PI control.
5. A focus on applications in fluctuating load environments such as electric vehicles and renewable energy systems, where dynamic motor parameters and environmental changes often occur.

Mathematical model of PMSM. In the dq-axis reference frame, disregarding the magnetic saturation effect, the extended back electromotive force (EMF) model of a PMSM can be represented as follows [4, 6, 24, 31]:

$$\begin{bmatrix} u_d \\ u_q \end{bmatrix} = \begin{bmatrix} R_s + sL_d & -\omega_e L_q \\ \omega_e L_q & R_s + sL_d \end{bmatrix} \cdot \begin{bmatrix} i_d \\ i_q \end{bmatrix} + e_a \cdot \begin{bmatrix} 0 \\ 1 \end{bmatrix}, \quad (1)$$

where s is the Laplace operator; u_d, u_q are the stator voltages in the dq-axis; i_d, i_q are the components of the stator current in the dq-axis; R_s is the stator winding resistance; L_d, L_q are the dq-axis inductances; ω_e is the rotational speed of the magnetic flux; e_a is the magnitude of the extended EMF of the PMSM, described as [1, 2, 24]:

$$e_a = \left(L_d - L_q\right)\omega_e i_d - \left(L_d - L_q\right)\frac{\mathrm{d}i_q}{\mathrm{d}t}. \quad (2)$$

Applying the inverse Park transformation to (1) yields the EMF model in the $\alpha\beta$-axis coordinate system, expressed as follows [6, 24]:

$$\begin{bmatrix} u_\alpha \\ u_\beta \end{bmatrix} = \begin{bmatrix} R_s + sL_d & -\omega_e\left(L_d - L_q\right) \\ \omega_e\left(L_d - L_q\right) & R_s + sL_d \end{bmatrix} \cdot \begin{bmatrix} i_\alpha \\ i_\beta \end{bmatrix} + e_a \cdot \begin{bmatrix} -\sin\theta \\ \cos\theta \end{bmatrix}, \quad (3)$$

where θ is the electrical rotor angle; u_α, u_β are the stator voltages in the $\alpha\beta$-axis; i_α, i_β are the components of the stator current in the $\alpha\beta$-axis.

The governing torque T_e equation can be derived from the input power equation of the windings. By simplifying this equation and applying the characteristics of the PMSM, the following expression is obtained [4, 32]:

$$T_e = \frac{3}{2} p\left\{\varphi_f i_q + \left(L_d - L_q\right) i_d i_q\right\}, \quad (4)$$

where p is the number of pole pairs; φ_f is the rotor permanent magnet flux linkage.

In a PMSM, the permanent magnets are positioned on the rotor's surface, making the motor non-salient. Consequently, the reluctance paths along both the d-axis and q-axis are identical, resulting in equal inductances for both axes. For simplicity, the machine's inductance will be represented by $L_d = L_q = L_s$. Therefore, (4) can be written as [33, 34]:

$$T_e = \frac{3}{2} p \varphi_f i_q. \quad (5)$$

Using Newton's second law, the mechanical equation of the system can be derived as:

$$T_e = T_L + j\frac{\mathrm{d}\omega_r}{\mathrm{d}t} + B_m\omega_r, \quad (6)$$

where j is the total system inertia; T_L is the load torque; ω_r is the mechanical angular velocity of the rotor; B_m is the viscous friction coefficient of the motor.

The total system inertia accounts for the inertia of the PMSM and all coupling or fastening components connecting them. The first term in the equation corresponds to the torque required to accelerate the system without the effects of friction. The other 2 terms refer to the torque needed to overcome viscous friction and disturbance torque, respectively. Disturbance torque can originate from factors such as load torque, unmodeled friction, or other dynamic effects within the system.

Load torque identification method. FFC is a control technique that improves system response to rapid input signal changes without relying on feedback from the system. This method effectively reduces delays and helps the control system stabilize quickly when there are sudden changes in load torque, disturbances, or external factors. FFC works by providing a control signal based on the predicted behavior of the system. When there are changes in load torque or external disturbances, the FFC control signal is computed and applied immediately without waiting for feedback from the system's sensors or measurement devices. To apply FFC, we first need to develop the dynamic model of the system. For SPMSM, this model describes the relationship between the electromagnetic torque, load torque and frictional effects within the system. From (6) we rewrite the general equation for the SPMSM system as follows:

$$j\frac{\mathrm{d}\omega_r}{\mathrm{d}t} = T_e - \underbrace{T_L - T_D}_{T_{L\_D}} - B_m\omega_r, \quad (7)$$

where T_L is the load torque acting on the motor, caused by external factors like mechanical load; T_D is the disturbance torque, including unmeasured factors such as unmodeled friction or external disturbances affecting the system. Angular acceleration $\mathrm{d}\omega_r/\mathrm{d}t$ is a key factor in determining how the motor system responds to the applied torque. The above equation can be restructured to calculate angular acceleration easily:

$$\begin{aligned} \frac{\mathrm{d}\omega_r}{\mathrm{d}t} &= \frac{1}{j}T_e - \frac{B_m}{j}\omega_r - \frac{1}{j}T_{L\_D}; \\ \frac{\mathrm{d}T_{L\_D}}{\mathrm{d}t} &= \tau_{L\_D}T_{L\_D} + w_{L\_D}, \end{aligned} \quad (8)$$

where τ_{L_D} is the attenuation coefficient; w_{L_D} is the noise affecting the load. Determining $\mathrm{d}\omega_r/\mathrm{d}t$ helps understand the rate of change of the motor's rotational angle under the influence of various factors such as electromagnetic torque, load torque and friction. The system can measure the ω_r but cannot directly measure T_{L_D}. Therefore, the speed sensor will give the result:

$$\omega_{meas} = \omega_r + v_{mot\_spd}, \quad (9)$$

where ω_{meas} is the measured motor speed; v_{mot_spd} is the measurement noise.

From (8), (9) we can rewrite in the form:

$$\begin{aligned} \begin{bmatrix} \frac{\mathrm{d}\omega_r}{\mathrm{d}t} \\ \frac{\mathrm{d}T_{L\_D}}{\mathrm{d}t} \end{bmatrix} &= A \cdot \begin{bmatrix} \omega_r \\ T_{L\_D} \end{bmatrix} + B \cdot T_e + C \cdot \begin{bmatrix} v_{mot\_spd} \\ w_{L\_D} \end{bmatrix}; \\ \omega_{meas} &= C \cdot \begin{bmatrix} \omega_r \\ T_{L\_D} \end{bmatrix} + v_{mot\_spd}, \end{aligned} \quad (10)$$

where $A = \begin{bmatrix} -B_m/j & -1/j \\ 0 & \tau_L \end{bmatrix}$; $B = \begin{bmatrix} 1/j \\ 0 \end{bmatrix}$; $G = \begin{bmatrix} 1 & 0 \\ 0 & 1 \end{bmatrix}$; $C = \begin{bmatrix} 1 & 0 \end{bmatrix}$.

From (7), it can be seen that the electromagnetic torque T_e must overcome the total load force and friction force to produce the angular acceleration of the motor. To calculate and control torque in the system, the drive system needs to respond to changes in the control signal and reference torque. The following equation can represent a dynamic model of the drive system:

$$\frac{\mathrm{d}T_e}{\mathrm{d}t} = \frac{1}{\tau_m}\left(T_{e\_ref} - T_e\right), \quad (11)$$

where T_{e_ref} is the reference torque that the system needs to achieve, provided by the controller, τ_m is the time constant of the drive system, which reflects the response speed of the drive system. This equation (11) means that the electromagnetic torque T_e will change over time and adjust to match the reference torque T_{e_ref}. The time response of the drive system is controlled τ_m, helping the system achieve stability when there are changes in the control signal.

FFC uses predictive models to react immediately to changes in load torque and disturbances. The FFC control signal $u(t)$ is calculated in advance and applied directly to the system to minimize delays:

$$u(t) = K_{FFC} \cdot T_{L\_D} + T_{e\_ref}, \quad (12)$$

where K_{FFC} is the gain constant for FFC. The FFC control signal $u(t)$ is calculated from the estimated load torque and disturbance torque, allowing the electromagnetic

torque to reach the desired value without waiting for feedback from the system.

Therefore, the modified system structure is depicted in Fig. 1. FFC helps transient response and eliminates interference in the control system. Figure 1 illustrates the control diagram of the system, integrating FOC to effectively manage the SPMSM. The speed controller takes the reference speed ω_{r_ref} as input and combines it with one of the 2 observers, using the torque signal T to generate the i_{qT_ref} signal for motor control. This signal, along with the feedback current in the dq-axis, creates the reference currents Δi_d and Δi_q. The current controller then produces the voltage commands u_d and u_q, which are converted into a 3-phase signal and supplied to the space vector pulse width modulation converter. The actual stator current i_q, the real position θ, obtained from the position sensor, and ω_r, derived from the derivative of the real position, are used as inputs for the feedback signal, the Luenberger observer, and the Kalman filter. The torque estimation methods are: discrete Luenberger observer in simulation 1 and discrete Kalman filter in simulation 2. These 2 simulations are independent of each other to test the response of the proposed controller against each observer. This design ensures that only one independent estimation method is active at any given time, thus avoiding data conflicts and facilitating the evaluation and comparison of the performance of both methods in a unified simulation framework.

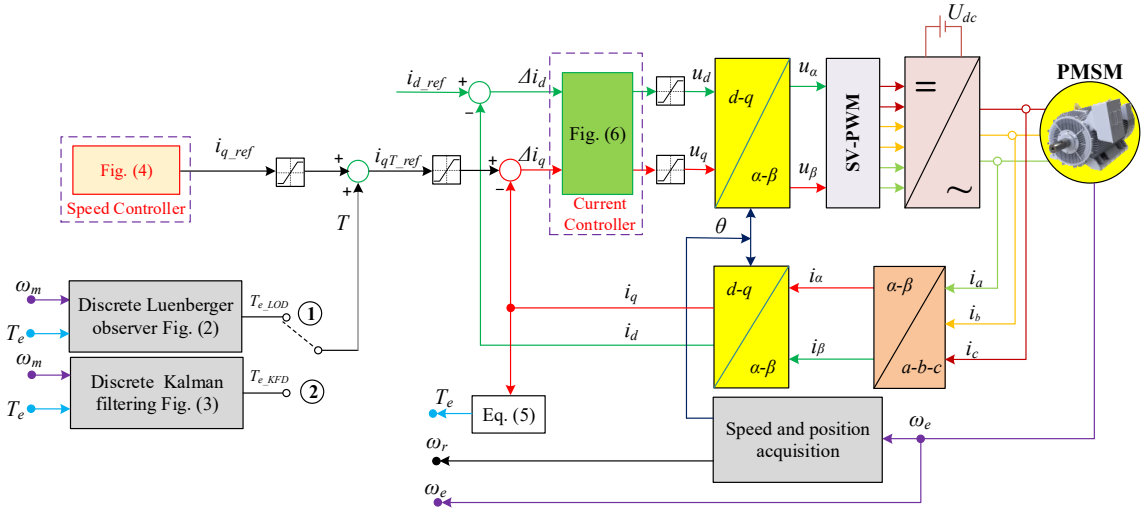

Fig. 1. Diagram of proposed control strategy

Design of discrete Luenberger observer. The basic structure of the Luenberger observer is shown in Fig. 2. Based on the mathematical model of the PMSM, the speed and torque of the PMSM, which are easy to measure, are typically used as inputs to reconstruct the motor's state. In Fig. 2 a feedback control is introduced, where the feedback signal is the difference between the estimated state and the actual state, such as the q-axis current. This feedback mechanism adjusts the observer to make the estimated value infinitely close to the actual value as time progresses. A linear state observer is constructed based on the mechanical equation of the system.

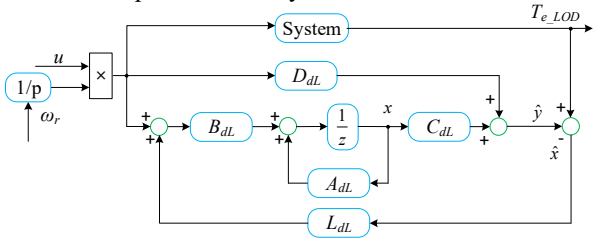

Fig. 2. Structure of the discrete Luenberger load observer

The plant in state-space form is presented in (13) [35–37]:

$$\begin{aligned} x &= Ax + Bu + Gw; \\ y &= Cx + Du + v, \end{aligned} \tag{13}$$

where in the Luenberger observer the matrices A, B, C, D, G are the essential components in the state-space model of the system. These matrices describe the system dynamics and the relationship between the system's states, inputs and outputs. With x representing the system states (such as speed and torque); u is the input, which is the actual motor torque T_e; w is the disturbance acting on the system; y is the output, which signals like speed or torque can measure.

The state space representation of the Luenberger observer is established in (10), we see that (13) is a shortened form of (10) to simplify the control system design process. The load is already transformed into a state. The Luenberger observer equation is used to estimate the states of the system. It is based on the system's dynamic model and adjusts the estimated states based on the measured outputs and inputs. The equation is given by [35, 38]:

$$\begin{aligned} \frac{d\hat{x}}{dt} &= A\hat{x} + Bu + L\cdot\left[y - \left(\hat{C}x + Du\right)\right]; \\ \frac{d\hat{x}}{dt} &= (A - LC)\cdot\hat{x} + \begin{bmatrix} B & L \end{bmatrix}\cdot\begin{bmatrix} u \\ y \end{bmatrix}; \\ \hat{y} &= C\hat{x}, \end{aligned} \tag{14}$$

where $\hat{x}$ is the estimated state of the system; L is the observer gain matrix; y is the measured output of the system.

The equation indicates that by designing the observer gains $L = [l_1 \quad l_2]^T$ such that the new system $(A - LC)$ becomes stable and fast enough, the estimation error can be driven to zero by using the estimated speed as a feedback signal ($\Delta\omega_r = \omega_{r\_ref} - \omega_r$), where ω_{r_ref} is the reference value and ω_r is the response rate. The observer gains L can be determined using the pole placement method. The closed-loop system poles are placed at the desired locations, and then the new characteristic equation

is derived. By comparing the coefficients of the latest and old characteristic equations, the observer gains can be found. By converting the above continuous state function A, B, C, D into a discrete state A_d, B_d, C_d, D_d, G_d and reconstructing the estimation matrices using the existing observer gain L, the values of the Luenberger observers are then A_{dL}, B_{dL}, C_{dL}, D_{dL}, G_{dL}. Hence the new system matrices are rewritten as:

$$\begin{aligned} &A_d = e^{At_s}; && \rightarrow A_{dL} = e^{A_d t_s}; \\ &B_d = \int_0^{t_s} e^{A.t} B \mathrm{d}t; && \rightarrow B_{dL} = \int_0^{t_s} e^{A_d t} B_d \mathrm{d}t; \\ &C_d = C; && \rightarrow C_{dL} = C_d; \\ &D_d = D; && \rightarrow D_{dL} = D_d; \\ &L_{dL} = G_{dL} S, \end{aligned} \tag{15}$$

where t_s is the sampling time; G_{dL} is the arbitrary matrix; S is obtained by solving the Sylvester equation.

The control parameters are given in Table 1.

Table 1

Discrete parameter values of the controller

Parameters	Value	Parameters	Value
$s_{1,2}$	$-50 \pm j10$	D_d	$\begin{bmatrix} 0.006 & 0.009 \\ 0 & -0.003 \end{bmatrix}$
τ_L	0	$t_s(s)$	$0.2 \cdot 10^{-3}$
L	$\begin{bmatrix} 99.885 \\ -37.960 \end{bmatrix}$	A_{dL}	$\begin{bmatrix} 0.980 & -0.013 \\ 0.007 & 0.999 \end{bmatrix}$
A_d	$\begin{bmatrix} 1 & -0.013 \\ 0 & 1.0 \end{bmatrix}$	B_{dL}	$\begin{bmatrix} 0.013 & 0.019 \\ 0 & -0.007 \end{bmatrix}$
B_d	$\begin{bmatrix} 0.013 \\ 0 \end{bmatrix}$	C_{dL}	$\begin{bmatrix} 0.990 & -0.006 \\ 0.003 & 1.0 \end{bmatrix}$
C_d	$\begin{bmatrix} 0.990 & -0.006 \\ 0.003 & 1.0 \end{bmatrix}$	D_{dL}	$\begin{bmatrix} 0.006 & 0.009 \\ 0 & -0.003 \end{bmatrix}$

Design of discrete steady-state Kalman filtering. This section presents a simple discrete Kalman filter. The system in discrete state space is represented as [24, 39, 40]:

$$\begin{aligned} x_k &= Ax_{k-1} + Bu_{k-1} + w_{k-1}; \\ y_k &= Cx_k + Du_k + v_k, \end{aligned} \tag{16}$$

where the subscript k–1, k are represented as the time step k–1 and k, respectively; x_k is the state vector; x_{k-1} is the vector state of the system; u_{k-1} is the system input; w_{k-1} is the process noise affecting the state; y_k is the output vector; y_k is the output vector at the time step k; v_k is the measurement noise affecting the output. The process noise w_k and measurement noise v_k are assumed to be white, zero-mean, uncorrelated, and have the following covariance properties [24, 39]:

$$\begin{aligned} &w_k \approx (0, Q_k); \quad v_k \approx (0, R_k); \\ &E\cdot\left[w_k v_j^T\right] = Q_k \delta_{k-1}; \; E\cdot\left[v_k v_j^T\right] = R_k \delta_{k-1}; \; E\cdot\left[w_k v_j^T\right] = 0, \end{aligned} \tag{17}$$

where Q_k is the covariance matrix of the process noise; R_k is the covariance matrix of the measurement noise; δ_{k-1} is the Kronecker delta function (equals 1 if $k = j$, otherwise 0).

Kalman filter algorithm, including initialization, state propagation, covariance update, and Kalman gain calculation. The process of solving this algorithm is presented as follows.

Initialization. The first step is to initialize the filter by defining the initial state estimate $\hat{x}_0^+$ as the expected value of the initial state x_0. Similarly, the state estimation error covariance matrix P_0^+ is initialized. These are described as [24, 39]:

$$\begin{aligned} &\hat{x}_0^+ = E\cdot(x_0); \\ &P_0^+ = E\cdot\left[\left(x_0 - \hat{x}_0^+\right)\cdot\left(x_0 - \hat{x}_0^+\right)^T\right]. \end{aligned} \tag{18}$$

State propagation. In this step, the filter propagates the state estimate forward in time. This is referred to as the prior state estimate in the literature. It is calculated using as [24, 39]:

$$\hat{x}_k^- = A\cdot\hat{x}_{k-1}^- + B\cdot u_{k-1}, \tag{19}$$

where $\hat{x}_k^-$ is the prior state estimate.

Covariance update. The next step is to update the state estimation error covariance matrix P_k^-, which describes the uncertainty in the state estimate. The equation for this update is [24, 39]:

$$P_k^- = A\cdot P_{k-1}^-\cdot A^T + Q_{k-1}, \tag{20}$$

where Q_{k-1} is the process noise covariance matrix.

Kalman gain calculation. Finally, the Kalman gain K_k is computed to determine how much the state estimate should be corrected based on the measurement error. The formula for this is [24, 39]:

$$K_k = \frac{P_k^-\cdot C^T}{P_k^-\cdot C\cdot C^T + R_k}. \tag{21}$$

The next step in the Kalman filter algorithm is the correction step, where the posterior state estimate $\hat{x}_k^+$ is updated based on the measurement. This process is described as [24, 39]:

$$\hat{x}_k^+ = \hat{x}_k^- + K_k\cdot\left(y_k - C\cdot\hat{x}_k^-\right). \tag{22}$$

The term $y_k - C\cdot\hat{x}_k^-$ is called the residual or innovation, representing the difference between the actual measurement and the predicted output. After updating the state estimate, the error covariance matrix P_k^+ is updated by [24, 39]:

$$P_k^+ = (I - C\cdot K_k)\cdot P_k^-, \tag{23}$$

where I is the identity matrix; $C{\cdot}K_k$ represents the adjustment to the covariance based on the Kalman gain and output matrix. It is expected that P_k^+ will decrease over time because the term $(I - C{\cdot}K_k) < 1$. This reduces uncertainty in the state estimate as more measurements are processed. The noise covariance matrices Q_k (process noise) and R_k (measurement noise) significantly affect the Kalman gain K_k. When Q_k increases, the state estimation error covariance P_k^- increases, leading to a higher Kalman gain K_k. Lowering R_k also increases the Kalman gain K_k. With a higher Kalman gain, the algorithm puts more weight on the new measurement, leading to larger corrections in the state estimate. Conversely, if K_k is close to 0, the algorithm ignores new measurements and assumes the current estimate is accurate. By substituting the same data as in the subsection of «design of discrete Luenberger observer», it gets the control parameters for the Kalman filter shown in Table 2.

Table 2

Discrete parameter values of the controller

Parameter	Value	Parameter	Value	Parameter	Value
$\hat{x}_k^-$	$\begin{bmatrix}125.686\\5.985\end{bmatrix}$	P_k^+	$\begin{bmatrix}0 & 0\\0 & 0.084\end{bmatrix}$	K_k	$\begin{bmatrix}0.835\\-0.556\end{bmatrix}$
Q_{k-1}	$\begin{bmatrix}0.001 & 0\\0 & 0\end{bmatrix}$	P_k^-	$\begin{bmatrix}0.001 & 0\\0 & 0\end{bmatrix}$	$\hat{x}_k^+$	$\begin{bmatrix}123.819\\0.966\end{bmatrix}$

In embedded systems, due to limitations in memory and computational resources, it is often preferable to fix the Kalman gain to reduce processing costs. This means that parameters K_k and P_k are not updated continuously, which is only feasible under the assumption that the system and noise remain time-invariant. The steady-state Kalman filter, although not fully optimal, approaches optimality $k\to\infty$. Figure 3 illustrates that the Kalman gain converges to a stable value after approximately 50 and 500 time samples, with a sampling time of 0.2 ms. In the left plot, the Kalman gain increases rapidly from 0.81 to 0.835 within the first 30 steps and then stabilizes, indicating quick adaptation to the measured signal. Meanwhile, the right plot shows the Kalman gain decreasing from –0.6 to near 0 over 500 steps, reflecting an increasing trust in system predictions over time. These variations enable the Kalman filter to enhance the accuracy of state estimation and noise reduction, effectively supporting the control of PMSMs.

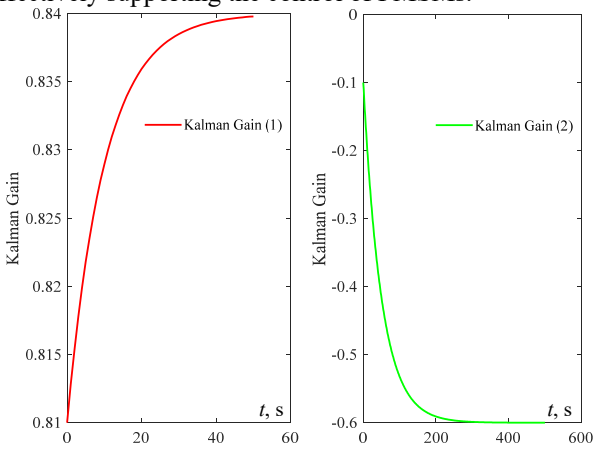

Fig. 3. Kalman gains captured during simulation

Proposed speed controller. To introduce the SMC design, we first define the system's state variables, which are crucial for implementing this control approach. By establishing these state variables, we can proceed to formulate the control law and analyze the system's behavior under SMC. Therefore, the system state is defined as:

$$\Delta\omega_r = \omega_{r\_ref} - \omega_r;$$
$$x_1 = \frac{\mathrm{d}(\Delta\omega_r)}{\mathrm{d}t} = -\frac{\mathrm{d}\omega_r}{\mathrm{d}t}. \tag{24}$$

Additionally, the following equations can be obtained based on (6) and (24):

$$\frac{\mathrm{d}(\Delta\omega_r)}{\mathrm{d}t} = -\frac{\mathrm{d}\omega_r}{\mathrm{d}t} = -\frac{p}{j}\cdot\left(\frac{3}{2}\cdot p\cdot\varphi_f\cdot i_q - T_L\right);$$
$$\frac{\mathrm{d}x_1}{\mathrm{d}t} = -\frac{\mathrm{d}^2(\Delta\omega_r)}{\mathrm{d}t^2} = -\frac{\mathrm{d}\omega_r}{\mathrm{d}t}\cdot\frac{3}{2}\cdot\frac{p^2}{j}\cdot\varphi_f\cdot\frac{\mathrm{d}i_q}{\mathrm{d}t}, \tag{25}$$

with $a = \frac{3}{2}\cdot\frac{p^2\cdot\varphi_f}{j}$, $u = \frac{\mathrm{d}i_q}{\mathrm{d}t}$, the system (25) is represented under the state space system as:

$$\frac{\mathrm{d}}{\mathrm{d}t}\begin{bmatrix}\Delta\omega_r\\x_1\end{bmatrix} = \begin{bmatrix}0 & 1\\0 & 0\end{bmatrix}\cdot\begin{bmatrix}\Delta\omega_r\\x_1\end{bmatrix} + u\cdot\begin{bmatrix}0\\-a\end{bmatrix}. \tag{26}$$

The sliding surface function is defined as:

$$s_s = c\cdot\Delta\omega_r + x_1. \tag{27}$$

Differentiating (27) becomes:

$$\frac{\mathrm{d}s_s}{\mathrm{d}t} = c\cdot\frac{\mathrm{d}(\Delta\omega_r)}{\mathrm{d}t} + \frac{\mathrm{d}x_1}{\mathrm{d}t} = c\cdot x_1 - a\cdot u. \tag{28}$$

According to the SMC law, the control signal is expressed as:

$$u = \frac{1}{a}\cdot\left(c\cdot x_1 + e\cdot|X|^{\alpha}\cdot\mathrm{sgn}(s_s) + k\cdot s_s\right), \tag{29}$$

where u is the control signal; c, e, k are the control parameters respectively; X is the state variable of the system; s_s is the deviation (or error) of the system from the sliding surface; α is the adaptive switching power term.

The reference current for the q-axis can be expressed as:

$$i_{q\_ref} = \int_0^T \frac{1}{a}\cdot\left(c\cdot x_1 + e\cdot|X|^{\alpha}\cdot\mathrm{sgn}(s_s) + k\cdot s_s\right)\mathrm{d}t. \tag{30}$$

To analyze the stability of the controller, define the Lyapunov function:

$$L_y = s_s^2/2. \tag{31}$$

Substituting (27) and (28) into (31), it has follows as:

$$\frac{\mathrm{d}L_y}{\mathrm{d}t} = s_s\cdot\left(c\cdot\Delta\omega_r + \frac{\mathrm{d}x_1}{\mathrm{d}t}\right) = -e\cdot|X|^{\alpha}\cdot|s_s| + k\cdot s_s^2. \tag{32}$$

The derivative of the Lyapunov function L_y gives us the above result, where $\mathrm{d}L_y/\mathrm{d}t$ is the change in the Lyapunov function over time. Since the parameters satisfy $e > 0$, $\alpha > 0$, $k > 0$, then $\mathrm{d}L_y/\mathrm{d}t < 0$ will be established, ensuring that the system enters the sliding mode as long as the conditions are met. SMC speed control diagram is shown in Fig. 4.

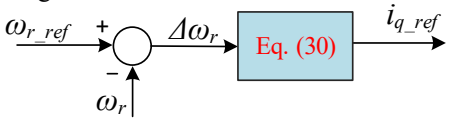

Fig. 4. The proposed speed control diagram

Proposed current controller. PRC is an effective control method designed to improve accuracy in control systems, especially in systems that require the resolution of issues related to steady-state error at the fundamental frequency. Unlike traditional PI control methods, PRC control is capable of adjusting the signal at the fundamental frequency without producing a steady-state error. PRC has the following transfer function:

$$G_{PRC}(s) = k_p + \frac{2\cdot k_i\cdot s}{s^2\cdot\omega_e^2}, \tag{33}$$

where k_p is the proportional gain; k_i is the integral gain; ω_e is the resonant frequency, which determines the frequency at which the PRC has the most effect.

When the angular frequency of the AC signal is given as ω_e, the magnitude of the transfer function $G_{PRC}(s)$ will be:

$$|G_{PRC}(s)|_{s=j\omega_e} = \sqrt{k_p^2 + \left(\frac{2\cdot k_i\cdot\omega_c}{-\omega_e^2+\omega_e^2}\right)^2}. \tag{34}$$

From (34), it can be observed that the magnitude of $G_{PRC}(s)$ becomes infinite, which allows the control of a

sinusoidal signal with the same frequency as the resonant frequency to achieve zero steady-state error control. However, in practical applications, due to issues in implementing the ideal PRC, this section uses an improved quasi-PRC, with its transfer function being:

$$G_{PRC}(s) = k_p + \frac{2 \cdot k_i \cdot \omega_e \cdot s}{s^2 + 2 \cdot \omega_c \cdot s + \omega_e^2}, \qquad (35)$$

where ω_c is the cutoff frequency of the quasi-resonant controller.

From (35), it can be seen that the controller has 3 design parameters: k_p, k_i and ω_c. For ease of analysis, assume that any 2 parameters are kept constant, and then observe how the variation of the 3rd parameter affects the system's performance. Figure 5 shows the corresponding changes in the Bode plot when only k_p, k_i and ω_c is changed, and analyzes the role of each parameter.

In Fig. 5,*a*, where k_p is changed, it can be seen that the magnitude outside the bandwidth increases as k_p increases, while the fundamental frequency does not increase significantly. This indicates that when k_p becomes too large, its effect on resonance is negligible. In Fig. 5,*b*, where only k_i is changed, it can be seen that as k_i increases, the gain at the fundamental frequency increases, indicating that it plays a role in eliminating steady-state error. However, the increase in k_i also widens the bandwidth of the PRC, thus increasing the influence of resonance and amplifying unnecessary signals, which is detrimental to the overall stability of the system. In Fig. 5,*c*, where only ω_c is changed, it can be seen that as ω_c decreases, the gain at the fundamental frequency increases, and the bandwidth narrows. This indicates that it has good selectivity for the signal, and f_e determines the bandwidth of the controller. Therefore, to achieve a good control effect with the resonant controller, the principle of parameter tuning is to adjust k_p to eliminate the steady-state error of the system and adjust ω_c to suppress the impact of frequency fluctuations. The transfer function (33) is in the *s*-domain. When using PRC for digital control of a 3-phase PMSM system, to simplify the discretization process, only the resonant controller is discretized. Its implementation can be done using bilinear transformation, and the transformation formula is:

$$s = \frac{1}{t_s} \cdot \frac{1 - z^{-1}}{1 + z^{-1}}. \qquad (36)$$

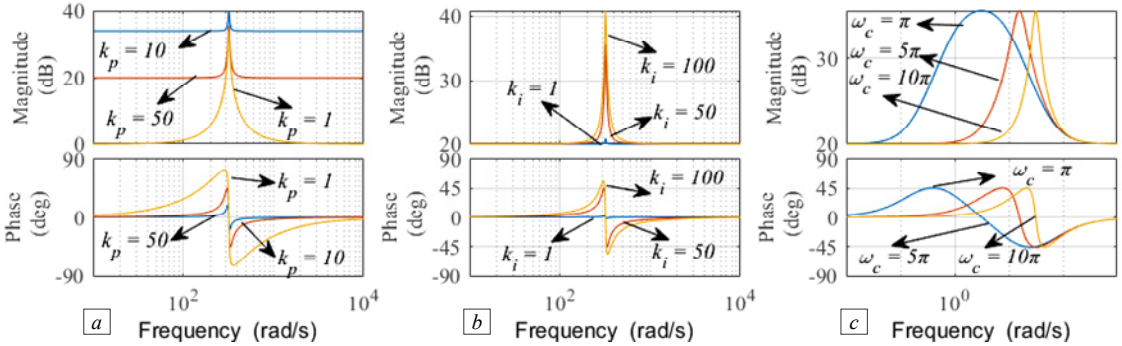

Fig. 5. The changes in the Bode plot corresponding: *a*) k_p is changed; *b*) k_i is changed; *c*) ω_c is changed

Substituting (36) into (35), it can become as follows:

$$G_{PRC}(z) = \frac{b_0 + b_1 z^{-1} + b_2 z^{-2}}{1 + a_1 z^{-1} + a_2 z^{-2}}, \qquad (37)$$

in which:

$$a_1 = \frac{2\omega_e^2 t_s^2 - 8}{4 + 4\omega_c t_s + \omega_e^2 t_s^2}; \quad a_2 = \frac{4 - 4\omega_c t_s + \omega_e^2 t_s^2}{4 + 4\omega_c t_s + \omega_e^2 t_s^2};$$

$$b_0 = \frac{4 k_i \omega_c t_s}{4 + 4\omega_e t_s + \omega_e^2 t_s^2}; \quad b_1 = 0; \quad b_2 = \frac{-4 k_i \omega_c t_s}{4 + 4\omega_c t_s + \omega_e^2 t_s^2}.$$

After organizing, the difference equation of the controller is:

$$u_{d,q}(k) = b_0 e(k) + b_2 e(k-2) - a_1 y(k-1) - a_2 y(k-2). \quad (38)$$

Equation (38) achieves steady-state control of the error signal. It can be seen that the control is relatively simple and easy to implement. The implementation block diagram of the PRC is shown in Fig. 6 and parameters are listed in Table 3.

Table 3

Parameter of the PRC

Parameter	Value	Parameter	Value
k_p	5.775	ω_c	20
k_i	1000	t_s	0.0001

We have the resonant frequency matches the motor speed, thus achieving near-error-free tracking of the current. Compared to traditional PI control methods, the control system based on the PR controller does not contain feed-forward compensation terms or decoupling terms related to motor parameters. This reduces coordinate rotation, thereby simplifying the implementation of the control algorithm and improving the robustness of the control system.

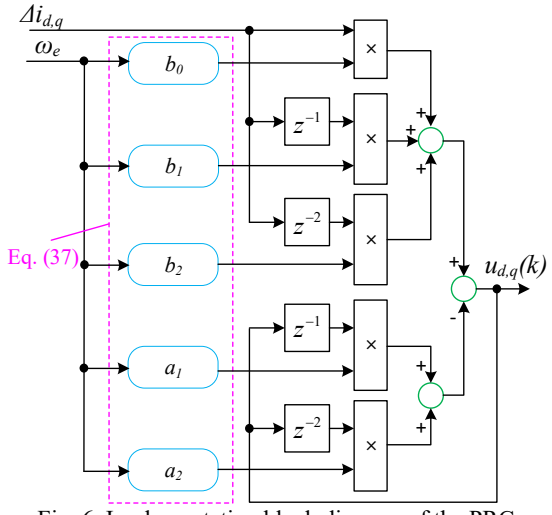

Fig. 6. Implementation block diagram of the PRC

Results and discussion. The simulation cases were conducted under steady-state conditions and assumed operating conditions to observe the control signals and performance between LSP and KSP under the influence of the proposed SMC-PRC controller and the traditional PI controller. The parameters of the SPMSM are listed in

Table 4. MATLAB/Simulink software was used to conduct 3 simulation experiments (Fig. 7), to demonstrate the operational capability of the SPMSM under all conditions and evaluate the effectiveness of the observation methods tested in this study. The data from the 3 conditions display key parameters, including the actual rotor speed, estimated speed, reference speed, current components, *dq*-axis voltage (i_d, i_q, u_d and u_q), and 3-phase current (i_{abc}). In each experimental case, the parameters were calculated and compared with the proposed SMC-PRC observer and the traditional PI controller. These values indicate the superiority of the proposed controller in this study.

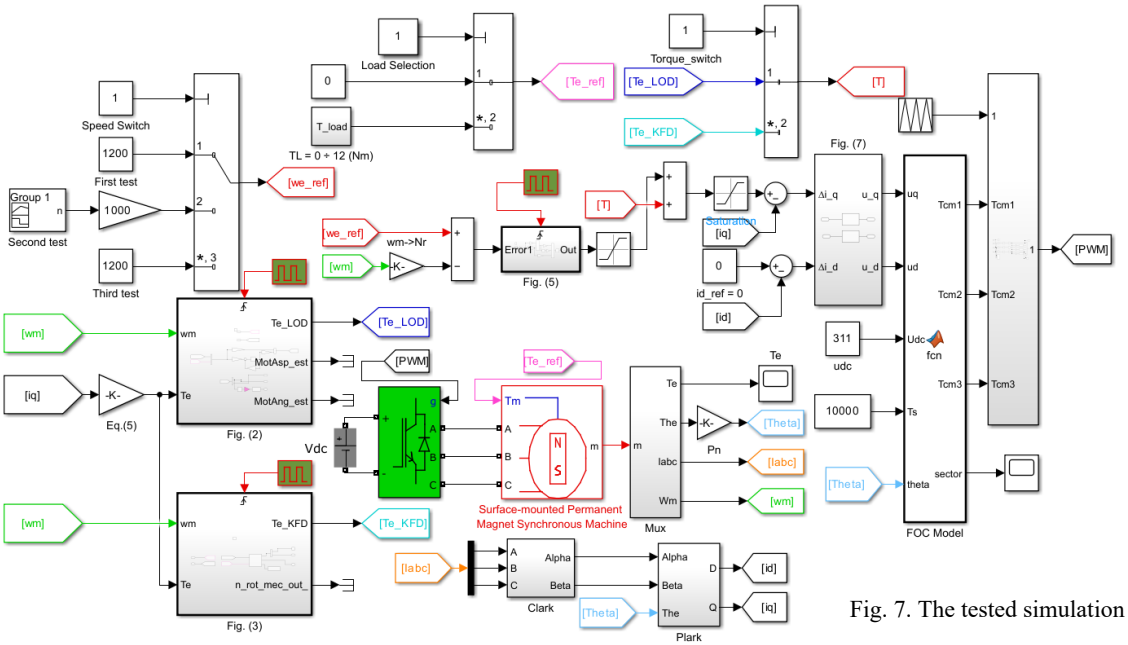

Fig. 7. The tested simulation model

Table 4

The parameters of tested system

Parameter	Value	Parameter	Value
Rated power P_r, kW	9.4	d-axis inductance L_d, mH	2.2
Rated speed n_r, rpm	4500	q-axis inductance L_q, mH	2.2
Number of pole pairs	4	Rotor peak PM flux linkage φ_m, Wb	0.12258
Stator resistance R_s, Ω	0.268	Viscous friction B_m, N·s/m	0.001665
Total inertia j, kg·m^2	0.0146	Rated torque T_r, N·m	20
DC-link voltage U_{dc}, V	360	Switching frequency f_s, kHz	5

Case study 1. In this experiment, 2 control strategies (SMC-PRC and PI) were compared when the motor operated at a low speed of 50 rpm and under no-load conditions. The simulation results showed that both control strategies were able to track the reference signal well (Fig. 8,*a*,*b*). However, during the startup process, the torque of SMC-PRC was lower compared to PI, with the startup values being 4.888 N·m and 12.994 N·m, respectively, as shown in Fig. 8,*c*,*d*. The startup currents also exhibited a significant difference: while SMC-PRC had a startup current of 6.649 A, PI had a much higher current – 17.671 A (Fig. 8,*e*,*f*). This indicates that SMC-PRC reduces the startup current by up to 62.382 %. Additionally, the 3-phase currents (Fig. 8,*g*,*h*), displayed distinct changes in both control strategies, with SMC-PRC providing a more stable current during startup.

The error indices IAE, ITAE, and ISE (Table 5) show that the SMC-PRC method significantly improves over PI, with IAE reduced by 10.837 %, ITAE – 9.6 %, ISE – 20.72 %.

Table 5

A comparison of the error indices in the case study 1

Observer type	SMC-PRC	PI	Ratios, %
IAE	0.3258	0.3654	10.837
ITAE	1.9548	2.1624	9.6
ISE	0.0176	0.0222	20.72

These results demonstrate that the use of the SMC-PRC controller not only helps reduce startup current but also enhances control performance, improving the accuracy and stability of the system compared to PI.

Case study 2. This test provides a comprehensive overview of the observed results when the speed command is increased from 2000 to 3000 rpm at 2 s and then reduced from 3000 rpm to 1000 rpm at 3 s, after which the motor stabilizes. The simulation results with both the SMC-PRC and PI controllers (Fig. 9) reveal significant differences in the control parameters throughout the operation. The speed of both controllers follows the reference signal almost exactly, but PI shows a slower settling time compared to SMC-PRC (Fig. 9,*a*,*b*). Based on the comparison of settling times between the 2 methods, SMC-PRC proves to be superior. Specifically, at 3000 rpm, the settling time of SMC-PRC is 2.089 s, which is shorter than PI's 2.265 s, and faster by approximately 0.176 s. At 2000 rpm, SMC-PRC has a settling time of just 0.165 s, while PI takes 0.568 s, faster by about 0.403 s. Finally, at 1000 rpm, SMC-PRC achieves a settling time of 3.186 s, while PI takes 3.63 s, faster by 0.444 s. In total, the settling time of SMC-PRC is 5.44 s, while PI's settling time is 6.463 s, with a difference of 1.023 s. Therefore, SMC-PRC is not only faster, but also enables the system to reach the reference speed more quickly and stably compared to PI. The torque in SMC-PRC during startup is 0.105 N·m, lower than PI's 0.343 N·m, indicating that SMC-PRC is more stable in the initial phase (Fig. 9,*c*,*d*). The startup currents i_q and i_d (Fig. 9,*e*,*f*) have values of 34.551 A and –15.355 A for SMC-PRC, significantly lower compared to PI's startup currents of 55.116 A and –17.964 A, indicating that SMC-PRC helps reduce the startup current by approximately 37.312 % for i_d and 14.634 % for i_q.

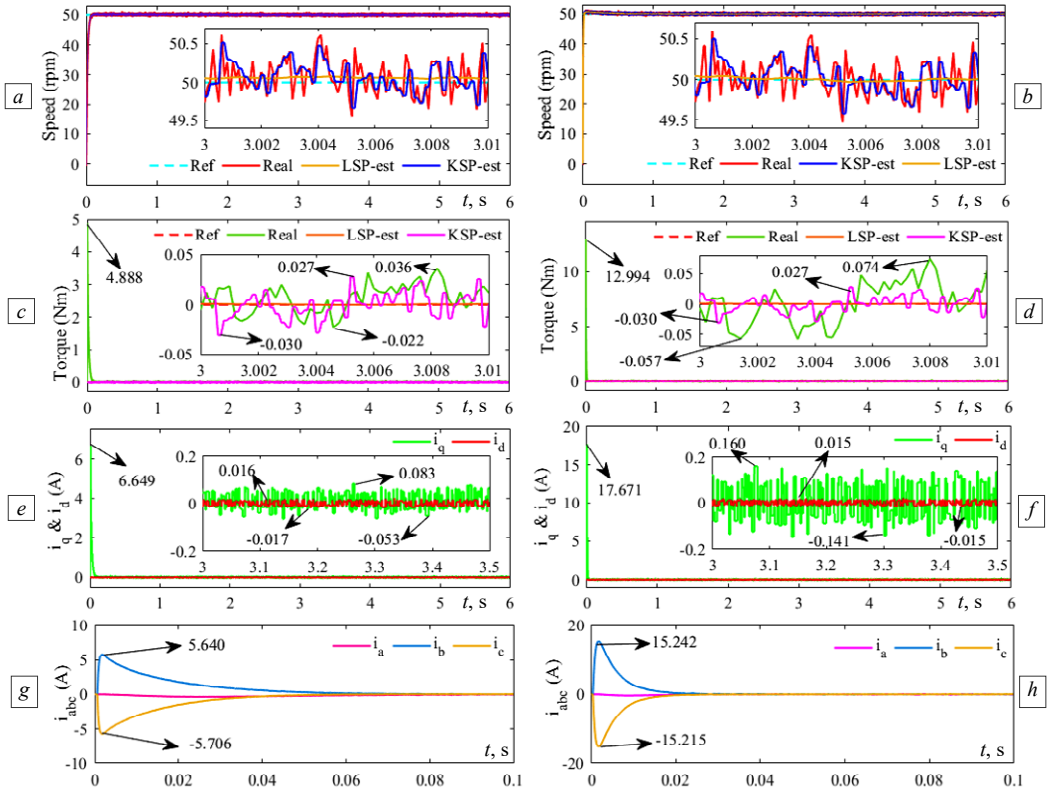

Fig. 8. Dynamic response of the system in the case study 1: *a*) and *b*) the rotor speed applying SMC-PRC and PI methods; *c*) and *d*) the electromagnetic torque applying SMC-PRC and PI methods; *e*) and *f*) the *d*- and *q*-axis current applying SMC-PRC and PI methods; *g*) and *h*) the 3-phase current applying SMC-PRC and PI methods

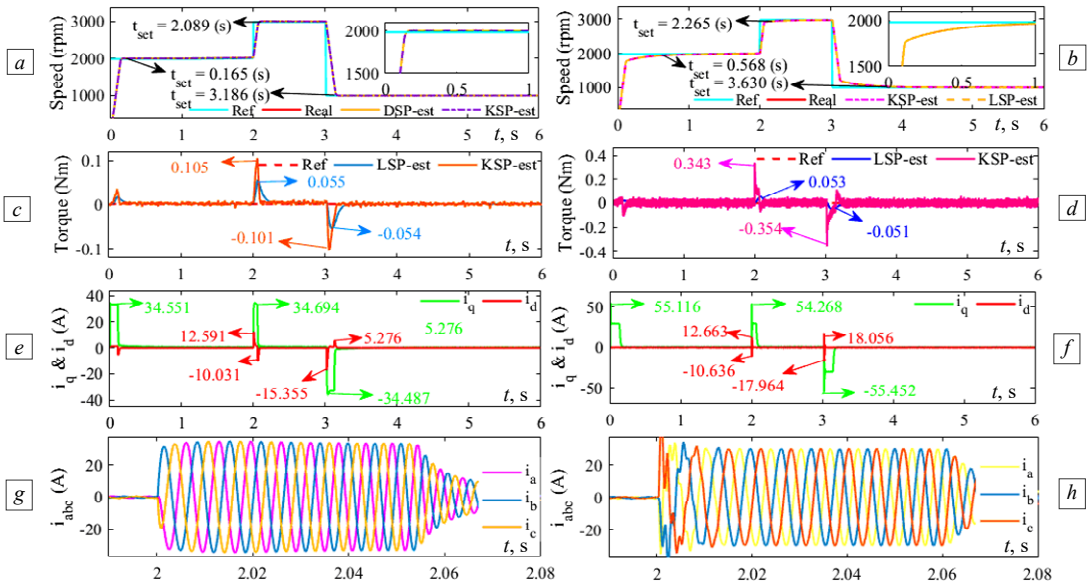

Fig. 9. Dynamic response of the system in the case study 2: *a*) and *b*) the rotor speed applying SMC-PRC and PI methods; *c*) and *d*) the electromagnetic torque applying SMC-PRC and PI methods; *e*) and *f*) the *d*- and *q*-axis current applying SMC-PRC and PI methods; *g*) and *h*) the 3-phase current applying SMC-PRC and PI methods

The 3-phase current images also show significantly greater stability in SMC-PRC compared to PI, where PI experiences strong oscillations in the phases. These results demonstrate that the SMC-PRC controller outperforms PI in reducing startup current and maintaining system stability.

The error indices IAE, ITAE, and ISE (Table 6) show significant improvements in the SMC-PRC method compared to PI, with IAE reduced by 94.614 %, ITAE – 94.603 %, and ISE – 99.708 %. These results confirm that the use of the SMC-PRC controller not only helps reduce the startup current, but also enhances control performance, improving the accuracy and stability of the system compared to PI.

Table 6

A comparison of the error indices in the case study 2

Observer type	SMC-PRC	PI	Ratios, %
IAE	0.548	10.182	94.614
ITAE	3.296	61.092	94.603
ISE	0.05	17.278	99.708

Case study 3. In this case, the simulation results were carried out by setting the speed to 2000 rpm and varying the load torque from 0 to 12 N·m at 3 s (Fig. 10). The results for both the SMC-PRC and PI control methods show significant differences in tracking the speed and current signals. Both methods maintain the speed close to the reference value, but SMC-PRC exhibits higher stability, especially during the

rapid speed change from 2.9 s to 3 s (Fig. 10,*a*,*b*). The torque in SMC-PRC stabilizes at around 12 N·m, while PI shows greater fluctuation, reaching approximately 12.53 N·m (Fig. 10,*c*,*d*). The currents in Fig. 10,*e*,*f* show large variations in both methods during startup. SMC-PRC starts with a significantly lower current about 18.558 A for i_q, while PI peaks at 20.229 A for i_q, indicating that SMC-PRC is more effective in reducing the startup current. Also, the 3-phase currents (Fig. 10,*g*,*h*), are more stable in SMC-PRC compared to PI, helping to minimize unnecessary oscillations. These results show that SMC-PRC not only reduces the startup current, but also improves the stability and overall performance of the system compared to PI.

The error indices IAE, ITAE, and ISE (Table 7) show that the SMC-PRC method significantly improves over PI, with IAE reduced by 74.18 %, ITAE – 74.18 %, and ISE – 93.333 %. These results confirm that the use of the SMC-PRC controller not only helps reduce the startup current but also enhances control performance, improving the accuracy and stability of the system compared to PI.

Table 7

A comparison of the error indices in the case study 3

Observer type	SMC-PRC	PI	Ratios, %
IAE	82.68	320.22	74.18
ITAE	496.08	1921.32	74.18
ISE	1139.33	17090.141	93.333

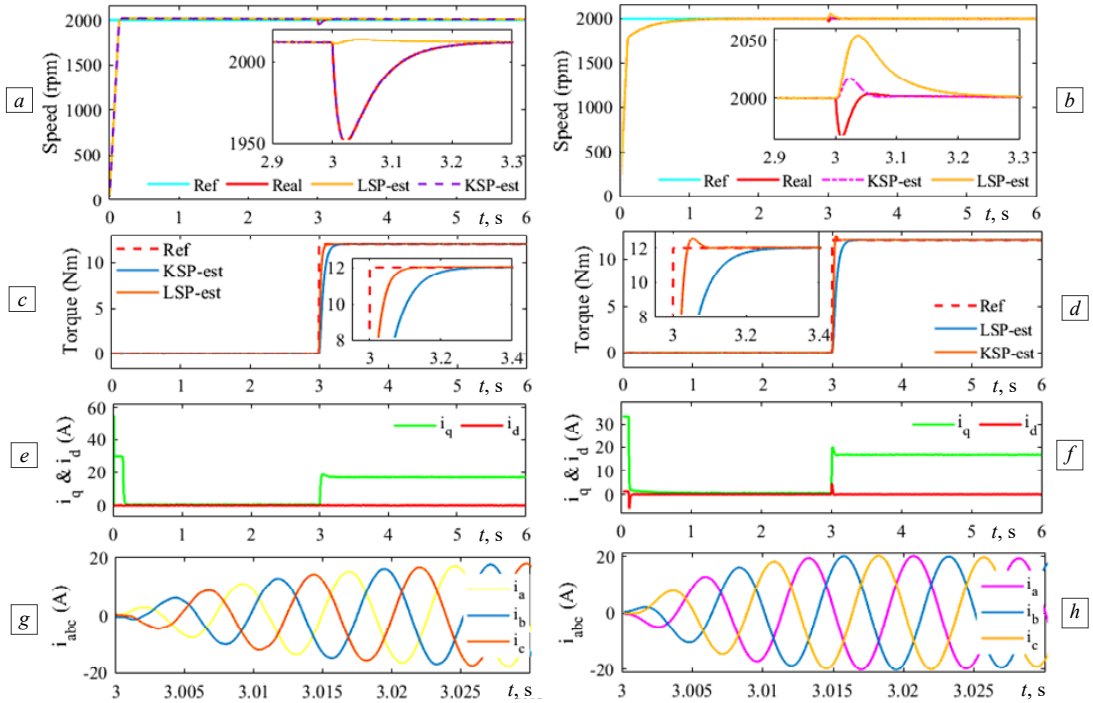

Fig. 10. Dynamic response of the system in the case study 3: *a*) and *b*) the rotor speed applying SMC-PRC and PI methods; *c*) and *d*) the electromagnetic torque applying SMC-PRC and PI methods; *e*) and *f*) the *d*- and *q*-axis current applying SMC-PRC and PI methods; *g*) and *h*) the 3-phase current applying SMC-PRC and PI methods

Conclusions. The purpose of this work was, firstly, to evaluate the performance of the use of field programmable gate array programmable logic circuits for the diagnosis of faults in an induction machine by introducing a fuzzy inference system into the algorithm of the analysis of the motor current signal analysis by taking the RMS signal of the stator phase current as the fault indicator signal. Secondly, to implement and validate the proposed hardware detection algorithm. The originality of our work has been to combine the performance of artificial intelligence techniques, the simplicity of motor current signal analysis algorithms and the execution power of programmable logic circuits, for the definition of a fault diagnosis structure for the induction machine achieving the best simplicity/performance and speed/performance ratios. Finally, the proposed solution has improved the performance of fault detection for the induction machine, especially in terms of hardware resource consumption, real-time online detection and speed of detection.

Conflict of interest. The authors declare that they have no conflicts of interest.

REFERENCES

1. Hassan A.M., Ababneh J., Attar H., Shamseldin T., Abdelbaset A., Metwally M.E. Reinforcement learning algorithm for improving speed response of a five-phase permanent magnet synchronous motor based model predictive control. *PLOS ONE*, 2025, vol. 20, no. 1, art. no. e0316326. doi: https://doi.org/10.1371/journal.pone.0316326.

2. Hu J., Yao Z., Xin Y., Sun Z. Design and optimization of the jet cooling structure for permanent magnet synchronous motor. *Applied Thermal Engineering*, 2025, vol. 260, art. no. 125051. doi: https://doi.org/10.1016/j.applthermaleng.2024.125051.

3. Liu F., Wang X., Sun L., Wei H., Li C., Ren J. Improved 3D hybrid thermal model for global temperature distribution prediction of interior permanent magnet synchronous motor. *Energy*, 2025, vol. 315, art. no. 134270. doi: https://doi.org/10.1016/j.energy.2024.134270.

4. Dien C.N., Nghia H.H.B. Optimizing Permanent Magnet Synchronous Motor Performance Considering Both Maximum Torque Per Ampere and Field Weakening. *International Journal of Intelligent Engineering & Systems*, 2025, vol. 18, no. 1, pp. 1121-1136. doi: https://doi.org/10.22266/ijies2025.0229.81.

5. Meng D., Wu Q., Zhang J., Li Y., Diao L. Restarting control of free-running interior permanent magnet synchronous motor under position sensorless control. *Alexandria Engineering Journal*, 2025, vol. 115, pp. 83-93. doi: https://doi.org/10.1016/j.aej.2024.11.111.

6. Liang Z., Cheng L., Cheng L., Li C. Rotor Position Estimation Algorithm for Surface-Mounted Permanent Magnet Synchronous Motor Based on Improved Super-Twisting Sliding Mode Observer. *Electronics*, 2025, vol. 14, no. 3, art. no. 436. doi: https://doi.org/10.3390/electronics14030436.

7. Alnaib I.I., Alsammak A.N. Optimization of fractional PI controller parameters for enhanced induction motor speed control via indirect field-oriented control. *Electrical Engineering & Electromechanics*, 2025, no. 1, pp. 3-7. doi: https://doi.org/10.20998/2074-272X.2025.1.01.

8. Mesloub H., Boumaaraf R., Benchouia M.T., Golea A., Golea N., Srairi K. Comparative study of conventional DTC and DTC_SVM based control of PMSM motor – Simulation and experimental results. *Mathematics and Computers in Simulation*, 2020, vol. 167, pp. 296-307. doi: https://doi.org/10.1016/j.matcom.2018.06.003.

9. Nemouchi B., Rezgui S.E., Benalla H., Nebti K. Fractional-based iterative learning-optimal model predictive control of speed induction motor regulation for electric vehicles application. *Electrical Engineering & Electromechanics*, 2024, no. 5, pp. 14-19. doi: https://doi.org/10.20998/2074-272X.2024.5.02.
10. Lee J., You S., Kim W., Moon J. Extended state observer-actor–critic architecture based output-feedback optimized backstepping control for permanent magnet synchronous motors. *Expert Systems with Applications*, 2025, vol. 270, art. no. 126542. doi: https://doi.org/10.1016/j.eswa.2025.126542.
11. Gu J., You S., Kim W., Moon J. Fuzzy Event-Triggered Super Twisting Sliding Mode Control for Position Tracking of Permanent Magnet Synchronous Motors Under Unknown Disturbances. *IEEE Transactions on Industrial Informatics*, 2023, vol. 19, no. 9, pp. 9843-9854. doi: https://doi.org/10.1109/TII.2022.3231410.
12. Aib A., Khodja D.E., Chakroune S., Rahali H. Fuzzy current analysis-based fault diagnostic of induction motor using hardware co-simulation with field programmable gate array. *Electrical Engineering & Electromechanics*, 2023, no. 6, pp. 3-9. doi: https://doi.org/10.20998/2074-272X.2023.6.01.
13. Gil J., You S., Lee Y., Kim W. Nonlinear sliding mode controller using disturbance observer for permanent magnet synchronous motors under disturbance. *Expert Systems with Applications*, 2023, vol. 214, art. no. 119085. doi: https://doi.org/10.1016/j.eswa.2022.119085.
14. Liu X., Wang Z., Wang W., Lv Y., Yuan B., Wang S., Li W., Li Q., Zhang Q., Chen Q. SMO-Based Sensorless Control of a Permanent Magnet Synchronous Motor. *Frontiers in Energy Research*, 2022, vol. 10, art. no. 839329. doi: https://doi.org/10.3389/fenrg.2022.839329.
15. Yao G., Wang X., Wang Z., Xiao Y. Senseless Control of Permanent Magnet Synchronous Motors Based on New Fuzzy Adaptive Sliding Mode Observer. *Electronics*, 2023, vol. 12, no. 15, art. no. 3266. doi: https://doi.org/10.3390/electronics12153266.
16. Yousefi-Talouki A., Pescetto P., Pellegrino G., Boldea I. Combined Active Flux and High-Frequency Injection Methods for Sensorless Direct-Flux Vector Control of Synchronous Reluctance Machines. *IEEE Transactions on Power Electronics*, 2018, vol. 33, no. 3, pp. 2447-2457. doi: https://doi.org/10.1109/TPEL.2017.2697209.
17. Pasqualotto D., Rigon S., Zigliotto M. Sensorless Speed Control of Synchronous Reluctance Motor Drives Based on Extended Kalman Filter and Neural Magnetic Model. *IEEE Transactions on Industrial Electronics*, 2023, vol. 70, no. 2, pp. 1321-1330. doi: https://doi.org/10.1109/TIE.2022.3159962.
18. Jiang F., Sun S., Liu A., Xu Y., Li Z., Liu X., Yang K. Robustness Improvement of Model-Based Sensorless SPMSM Drivers Based on an Adaptive Extended State Observer and an Enhanced Quadrature PLL. *IEEE Transactions on Power Electronics*, 2021, vol. 36, no. 4, pp. 4802-4814. doi: https://doi.org/10.1109/TPEL.2020.3019533.
19. Zhang Y., Yin Z., Bai C., Wang G., Liu J. A Rotor Position and Speed Estimation Method Using an Improved Linear Extended State Observer for IPMSM Sensorless Drives. *IEEE Transactions on Power Electronics*, 2021, vol. 36, no. 12, pp. 14062-14073. doi: https://doi.org/10.1109/TPEL.2021.3085126.
20. Zhang G., Wang G., Xu D., Zhao N. ADALINE-Network-Based PLL for Position Sensorless Interior Permanent Magnet Synchronous Motor Drives. *IEEE Transactions on Power Electronics*, 2016, vol. 31, no. 2, pp. 1450-1460. doi: https://doi.org/10.1109/TPEL.2015.2424256.
21. Kim H., Son J., Lee J. A High-Speed Sliding-Mode Observer for the Sensorless Speed Control of a PMSM. *IEEE Transactions on Industrial Electronics*, 2011, vol. 58, no. 9, pp. 4069-4077. doi: https://doi.org/10.1109/TIE.2010.2098357.
22. Wu C., Sun X., Wang J. A Rotor Flux Observer of Permanent Magnet Synchronous Motors With Adaptive Flux Compensation. *IEEE Transactions on Energy Conversion*, 2019, vol. 34, no. 4, pp. 2106-2117. doi: https://doi.org/10.1109/TEC.2019.2932787.
23. Xu W., Jiang Y., Mu C., Blaabjerg F. Improved Nonlinear Flux Observer-Based Second-Order SOIFO for PMSM Sensorless Control. *IEEE Transactions on Power Electronics*, 2019, vol. 34, no. 1, pp. 565-579. doi: https://doi.org/10.1109/TPEL.2018.2822769.
24. Yingjun S., Zhenglong W., Yuanyuan F. An adaptive extended Kalman filter observer-for permanent magnet synchronous motor position sensorless control systems. *Scientific Reports*, 2025, vol. 15, no. 1, art. no. 11605. doi: https://doi.org/10.1038/s41598-025-85787-5.
25. Salvatore N., Caponio A., Neri F., Stasi S., Cascella G.L. Optimization of Delayed-State Kalman-Filter-Based Algorithm via Differential Evolution for Sensorless Control of Induction Motors. *IEEE Transactions on Industrial Electronics*, 2010, vol. 57, no. 1, pp. 385-394. doi: https://doi.org/10.1109/TIE.2009.2033489.
26. Zerdali E., Barut M. The Comparisons of Optimized Extended Kalman Filters for Speed-Sensorless Control of Induction Motors. *IEEE Transactions on Industrial Electronics*, 2017, vol. 64, no. 6, pp. 4340-4351. doi: https://doi.org/10.1109/TIE.2017.2674579.
27. Yin Z., Xiao L., Sun X., Liu J., Zhong Y. A speed and flux estimation method of induction motor using fuzzy extended Kalman filter. *2014 International Power Electronics and Application Conference and Exposition*, 2014, pp. 693-698. doi: https://doi.org/10.1109/PEAC.2014.7037941.
28. Wang T., Huang S., Gao M., Wang Z. Adaptive Extended Kalman Filter Based Dynamic Equivalent Method of PMSG Wind Farm Cluster. *IEEE Transactions on Industry Applications*, 2021, vol. 57, no. 3, pp. 2908-2917. doi: https://doi.org/10.1109/TIA.2021.3055749.
29. Zerdali E. Adaptive Extended Kalman Filter for Speed-Sensorless Control of Induction Motors. *IEEE Transactions on Energy Conversion*, 2019, vol. 34, no. 2, pp. 789-800. doi: https://doi.org/10.1109/TEC.2018.2866383.
30. Simon D. *Optimal State Estimation: Kalman, H∞, and Nonlinear Approaches*. John Wiley & Sons, 2006. 526 p. doi: https://doi.org/10.1002/0470045345.
31. Saberi S., Rezaie B. Sensorless FCS-MPC-based speed control of a permanent magnet synchronous motor fed by 3-level NPC. *Journal of Renewable Energy and Environment*, 2021, vol. 18, no. 2, pp. 13-20. doi: https://doi.org/10.30501/JREE.2020.234039.1118.
32. Abu Ibaid O.Z.I., Belhamdi S., Abid M., Chakroune S., Mouassa S., Al-Sagar Z.S. Wavelet packet analysis for rotor bar breakage in an inverter induction motor. *Electrical Engineering & Electromechanics*, 2023, no. 3, pp. 3-11. doi: https://doi.org/10.20998/2074-272X.2023.3.01.
33. Kuvvetli I., Tap A., Ergenc A.F., Ergene L.T. An adaptive neurofuzzy inference system controller design of an SPMSM drive for multicopter applications. *Transactions of the Institute of Measurement and Control*, 2024, pp. 1-15. doi: https://doi.org/10.1177/01423312241286042.
34. Kimouche A., Mekideche M.R., Chebout M., Allag H. Influence of permanent magnet parameters on the performances of claw pole machines used in hybrid vehicles. *Electrical Engineering & Electromechanics*, 2024, no. 4, pp. 3-8. doi: https://doi.org/10.20998/2074-272X.2024.4.01.
35. Boudouani S., Yahdou A., Benbouhenni H., Boudjema Z., Almalki M.M., Alghamdi T.A. Enhanced speed sensorless control of IPMSM using integral synergetic observer. *Measurement and Control*, 2025, pp. 1-15. doi: https://doi.org/10.1177/00202940241312846.
36. Caramori G.M., De Almeira L.M.M., Da Costa C. Enhanced Position Estimation of PMSM Using the Luenberger Observer and PLL Algorithm: Design and Simulation Study. *European Journal of Engineering and Technology Research*, 2023, vol. 8, no. 6, pp. 37-44. doi: https://doi.org/10.24018/ejeng.2023.8.6.3122.
37. Saifi R. Implementation of a new flux rotor based on model reference adaptive system for sensorless direct torque control modified for induction motor. *Electrical Engineering & Electromechanics*, 2023, no. 2, pp. 37-42. doi: https://doi.org/10.20998/2074-272X.2023.2.06.
38. Moussaoui L., Aouaouda S., Rouaibia R. Fault tolerant control of a permanent magnet synchronous machine using multiple constraints Takagi-Sugeno approach. *Electrical Engineering & Electromechanics*, 2022, no. 6, pp. 22-27. doi: https://doi.org/10.20998/2074-272X.2022.6.04.
39. Dilys J., Stankevič V., Łuksza K. Implementation of Extended Kalman Filter with Optimized Execution Time for Sensorless Control of a PMSM Using ARM Cortex-M3 Microcontroller. *Energies*, 2021, vol. 14, no. 12, art. no. 3491. doi: https://doi.org/10.3390/en14123491.
40. Rouaibia R., Djeghader Y., Moussaoui L. Artificial neural network and discrete wavelet transform for inter-turn short circuit and broken rotor bars faults diagnosis under various operating conditions. *Electrical Engineering & Electromechanics*, 2024, no. 3, pp. 31-37. doi: https://doi.org/10.20998/2074-272X.2024.3.04.

Received 01.05.2025
Accepted 13.07.2025
Published 02.11.2025

V.T.K. Nhi[1]*, Postgraduate Student, Lecturer,*
B.T. Quy[1]*, PhD,*
H.H.B. Nghia[1]*, College Student,*
L.V. Dai[1]*, PhD,*
[1] Faculty of Electrical Engineering Technology,
Industrial University of Ho Chi Minh City, Vietnam,
e-mail: levandai@iuh.edu.vn (Corresponding Author)

How to cite this article:
Nhi V.T.K., Quy B.T., Nghia H.H.B., Dai L.V. A robust hybrid control strategy for enhancing torque stability and performance in PMSM drives. *Electrical Engineering & Electromechanics*, 2025, no. 6, pp. 64-74. doi: https://doi.org/10.20998/2074-272X.2025.6.09